

Segmenting multiple overlapping objects via a Hybrid Active Contour Model incorporating Shape Priors: Applications to Digital Pathology

Sahirzeeshan Ali^a and Anant Madabhushi^b

^aDepartment of Electrical and Computer Engineering, Rutgers University, USA;

^bDepartment of Biomedical Engineering, Rutgers University, USA

ABSTRACT

Active contours and active shape models (ASM) have been widely employed in image segmentation. A major limitation of active contours, however, is in their (a) inability to resolve boundaries of intersecting objects and to (b) handle occlusion. Multiple overlapping objects are typically segmented out as a single object. On the other hand, ASMs are limited by point correspondence issues since object landmarks need to be identified across multiple objects for initial object alignment. ASMs are also constrained in that they can usually only segment a single object in an image. In this paper, we present a novel synergistic boundary and region-based active contour model that incorporates shape priors in a level set formulation. We demonstrate an application of these synergistic active contour models using multiple level sets to segment nuclear and glandular structures on digitized histopathology images of breast and prostate biopsy specimens. Unlike previous related approaches, our model is able to resolve object overlap and separate occluded boundaries of multiple objects simultaneously. The energy functional of the active contour is comprised of three terms. The first term comprises the prior shape term, modeled on the object of interest, thereby constraining the deformation achievable by the active contour. The second term, a boundary based term detects object boundaries from image gradients. The third term drives the shape prior and the contour towards the object boundary based on region statistics. The results of qualitative and quantitative evaluation on 100 prostate and 14 breast cancer histology images for the task of detecting and segmenting nuclei, lymphocytes, and glands reveals that the model easily outperforms two state of the art segmentation schemes (Geodesic Active Contour (GAC) and Roussons shape based model) and resolves up to 92% of overlapping/occluded lymphocytes and nuclei on prostate and breast cancer histology images.

1. INTRODUCTION

Statistical Shape Models (SSM)¹ and Active Contours have been used heavily to segment objects of interest in an array of applications involving biomedical imaging.^{2,3} A fundamental problem when computing SSMs is the determination of correspondences between training instances of the object of interest, especially when the surfaces are represented by point clouds.¹ Often, homologies between the points are assumed which might lead to an imprecise model of the shape. A number of deformable segmentation schemes have been developed to date. They can be divided into two categories: boundary-based and region-based. The boundary-based approaches such as geodesic/geometric active contours have become popular on account of their reliable performance and fast computation.^{4,11,12} However, as only the edge information is utilized, their performance is limited by the strength of the image gradient. These models are typically unable to handle object occlusion or scene clutter. Region based approaches rely on statistics obtained from the entire region; color or textural attributes being often employed to detect the object.¹⁰ However, these models typically require far more computations and like the boundary based approaches are limited in their ability to deal with object occlusions and scene clutter. The integration of prior shape knowledge of the objects for segmentation tasks represents a natural way to solve occlusion problems.^{5,6} Combining a statistical shape prior with geometric/geodesic active contours via a variational model allows for simultaneous registration and segmentation.⁶ A limitation of these third generation

Further author information: (Send correspondence to Sahir Ali or Anant Madabhushi)

Sahir Ali: E-mail: sahirali@eden.rutgers.edu (or sahirali30@gmail.com), Telephone: 732-445-4500 (ext.6261)

Anant Madabhushi: E-mail: anantm@rci.rutgers.edu, Telephone: 732-445-4500 (ext.6213)

active contours, however, is that they introduce shape priors into a level set framework in such a way that usually only one pair of overlapping objects can be accurately resolved into independent shapes within an image scene.^{5,9}

In the rapidly emerging field of digital pathology, the ability to segment multiple objects, especially the ability to deal with object overlap and occlusion is highly critical in the context of a number of different diagnostic and prognostic applications.^{18,19} Currently, the diagnosis of diseases such as prostate and breast cancer is done manually by visual analysis of tissue samples, typically obtained from a patient via biopsy.^{3,14} The architectural arrangement of nuclear and glandular structures on histopathology is highly relevant in the context of disease grading.^{3,13,14} Cancer grade in the context of breast and prostate cancer is a key feature used to predict patient prognosis and in prescribing a treatment.¹⁸ While grading systems exist in the context of both breast and prostate cancer, manual grading is time consuming and prone to human errors due to observer variability and can lead to variable prognosis and suboptimal treatment. Automated segmentation and quantification of nuclear and glandular structures is critical for classification and grading of cancer.^{3,14} In the context of prostate cancer (CaP), pathologists grade histopathological specimens by visually characterizing gland morphology and architecture in regions they suspect are malignant. The Gleason grading system is used to describe CaP aggressiveness; lower gleason grade structures such as glands are medium-sized with round shapes, while in higher gleason grade pattern, glands tend to be small and have irregular shapes. Doyle, et al.¹³ showed that spatial graphs (eg. Voronoi, Delaunay, minimum spanning tree) built using nuclei as vertices in digitized histopathology images, yielded a set of quantitative feature that allowed for improved separation between intermediate gleason patterns. Veltri, et al.² showed that nuclear shape and morphology was reflective of disease aggressiveness and patient outcome. Both of these methods require accurate segmentation of prostate nuclei as an initial step, but had previously employed manual or semi-automated approaches.

Lymphocyte Infiltration (LI) has been identified as an important prognostic marker of outcome in Her2+ breast cancer and in other diseases as well.^{14,17} Lymphocyte segmentation in hematoxylin and eosin (H&E) stained BC histopathology images is complicated by the similarity in appearance between lymphocyte nuclei and other structures (e.g., cancer nuclei) in the image. This may lead to incorrect determination of the extent of LI. Automated detection and quantification of these structures on histopathology imagery could potentially result in the development of a digital prognostic tool for predicting patient outcome (and hence deciding treatment strategies).

However, an automated lymphocyte or nuclear detection algorithm on H&E images has to be able to deal with the (1) variability in digital slide appearance due to inconsistencies in histological staining, (2) poor image quality with tissue samples due to slide digitization, and (3) tissue fixation. Moreover, LI may be characterized by a high density of lymphocytes or nuclei, which could cause significant overlap among lymphocyte nuclei and other structures on the H&E images. This often results in adjacent nuclei visually appearing as one single lymphocyte. Basavanthally, et al. quantified the extent of lymphocytic infiltration (LI) in HER2+ breast cancers using a nuclear detection and graph feature based approach.¹⁴ Fatakdwala, et al.³ combined expectation maximization scheme with an explicit concavity based overlap resolution scheme to separate overlapping lymphocytic nuclei.

In this paper, we present a novel synergistic boundary and region-based active contour model that incorporates shape priors in a level set formulation. We demonstrate an application of these synergistic active contour models using multiple level sets to segment nuclear and glandular structures on digitized histopathology. Our novel scheme can segment nuclear and glandular structures in breast and prostate cancer H&E histopathology imagery and has the ability to detect and segment all of the overlapping lymphocytes and nuclei simultaneously.

2. PREVIOUS RELATED WORK AND NOVEL CONTRIBUTIONS

The basic idea behind the active contour model (AC), such as introduced by Kass et al.⁴ is the following: the segmentation of any object in a given image \mathcal{C} , which is well discernible and whose edges can be described by a closed curve, is equivalent to the location of sharp image intensity variations by iteratively deforming a curve C towards the edges of the object. Such a model is entirely dependent on the chosen parametrization of the initial curve $C(p) = (x(p), y(p)) \in \Omega, p \in [0, 1]$. Caselles, et al.¹¹ proposed to solve the parametrization dependency problem with the Geodesic Active Contour (GAC) model. They introduced a new intrinsic energy functional which is independent of the initial curve parametrization, and minimization of which results in a

geodesic in Riemannian space. The associated evolution equation can be written as $\partial_t C = F \cdot \mathcal{N}$ where F is a speed term derived from an energy functional and \mathcal{N} is the exterior unit normal vector to the curve C . To deal with topological changes, the evolution curve is handled by the level set method introduced by Osher and Sethian.¹⁵ The idea is to represent the curve as the level zero of a higher dimensional function ϕ (which is often a signed distance function). This level set function will evolve in time following $\partial_t \phi = F \cdot |\Delta \phi|$ and the interface at the level zero corresponds to the model's evolving contour. AC models^{4,11} based on edge/boundary detection have been previously proposed and these are typically referred to as the first generation of active contours. However, edge-based active contours are very sensitive to noise and require careful initialization. To deal with these problems, segmentation models based on region statistics such as mean, variance, and probability density functions (PDFs) have been developed. Chan and Vese⁶ proposed a 2-phase segmentation method based on the mean descriptor where the AC evolves in such a way that the difference between the gray level intensity average between the foreground and the background was maximized.

In their seminal work, Cootes, et al.¹ proposed to use principal component analysis (PCA) to capture the main shape variations of parametric AC's (active shapes) within a training set and thus to represent the prior shape information. Consequently, their model is not parametrization free. Leventon, et al.⁵ proposed the introduction of prior shape information into AC, intrinsically represented by level set functions, the core idea being to apply PCA on the signed distance functions (SDF) of the parametric GACs. This feature allowed them to construct an intrinsic and parametrization free shape model. The shape prior is then composed of the mean level set shape and a weighted sum of the m strongest eigen modes of variation (obtained from the PCA of the SDFs). SDFs have the additional advantage that they are more robust to slight misalignments of the training sequence compared to parametric curves. Unfortunately, the shape functions resulting from a PCA are not exactly SDFs, as proved by Leventon, et al.,⁵ but they can nonetheless be used in practice since they are very close to real SDFs. Rousson, et al.⁸ proposed a method where the optimal weight factors of the eigenmodes of variation are estimated by solving a linear system. Bresson, et al.⁹ have integrated the geometric shape prior of Leventon, et al. into the segmentation framework based on AC as well as on a region driven term derived from the Chan and Vese energy term.⁶ In,^{7,8} the signed distance functions of the training images are computed and the statistics of the signed distance training set is captured via PCA. This representation assumes that the PDF of the training set is Gaussian.

In this work, the contours that segment the object-boundaries are represented using the level set method, and are evolved by minimizing the variational energy. The novel methodological contribution of this work is to learn the shape prior for the target object of interest (nuclei and glands in our application) and apply it into hybrid AC model to segment all the overlapping and non-overlapping objects simultaneously. Under the level set framework, the contour is represented implicitly as the zero level of a higher dimensional embedding function, and the contour propagation is performed by evolving the embedding function. This enables one to handle topological changes of the boundary such as splitting and merging easily. Unlike previous related work,^{6,8,9} our framework is able to handle simultaneous segmentation of multiple objects. We present an application of our model for the problem of segmenting multiple, overlapping, and intersecting nuclei and lymphocytes from a total of 114 images from breast and prostate cancer datasets. The ground truth for quantitative evaluation was provided in the form of nuclear and glandular boundaries by expert pathologists.

3. SHAPE MODEL FORMULATION

An image is defined as $\mathcal{C} = (\mathbf{C}, \mathbf{f})$ where \mathbf{C} is a 2D grid representing pixels $c \in \mathbf{C}$, with $c = (x, y)$ representing the Cartesian coordinates of a pixel and f is a function that assigns a three element vector to c and is defined as $f(c) \in \mathbb{R}^3$. For gray scale or scalar images, f_g assigns intensity values to $c \in \mathbf{C}$ and is defined as $f_g(c) \in \mathbb{R}$.

3.1 Shape Alignment

The collected shapes are aligned first to the same position, orientation, and scale. The level set functions of the training shapes are employed for the purposes of model training. A shape prior model is constructed using statistical methods.⁵ In this paper, we only consider objects whose shapes are either view-angle independent or less affected by view angles. Hence the training shapes are only subject to affine transformations such as

Table 1. Description of notation and commonly used symbols in this paper.

| Symbol | Description | Symbol | Description |
|---------------|---|----------------------|---|
| \mathcal{C} | 2D image scene | \mathbf{C} | 2D Cartesian grid of pixels $c = (x, y)$ |
| $f(c)$ | function that assigns intensity values to pixel c | S | the shape contour (zero level set) |
| \mathbb{C} | the zero level set $\mathbb{C} = \{c \in \Omega : \phi(c) = 0\}$ | Ω | bounded open set in \mathbb{R}^2 |
| $H(\phi)$ | Heavside function $H(\phi) = \begin{cases} 1, & \phi(c) \geq 0; \\ 0, & \phi(c) < 0. \end{cases}$ | $\delta(\phi)$ | Delta function $\delta(\phi) = \begin{cases} +\infty, & \phi(c) = 0; \\ 0, & \phi(c) \neq 0. \end{cases}$ |
| Ω_f | foreground region $\Omega_f = \{c \in \Omega : \phi(c) > 0\}$ | Ω_b | background region $\Omega_b = \{c \in \Omega : \phi(c) < 0\}$ |
| $\phi(c)$ | the level set function | $\mathcal{A}(\cdot)$ | the set of pixels within boundary |
| ψ | the shape function | u_{in}, u_{out} | partitioned foreground and background regions |

translation, rotation and scale. A simple alignment method, the Euclidean similarity transformation (EST) defined as A_s , is adopted for this work. An EST of a point x_p into a point x'_p is defined by the transformation

$$x'_p = \alpha R x_p + T \quad (1)$$

where α is the isotropic scaling factor, R is the rotation matrix, and T is the translation vector. For each training shape, the set of parameters (α, R, T) needs to be found to adjust it to the same pose as a predefined (usually arbitrary selected) reference shape. We determine these parameters in the following ways:

- *Translation T* : Obtained by computing the distance between the centroid of target shape (x_i, y_i) and the centroid of reference shape (x_j, y_j)

$$T = \sqrt{(x'_i - x_j)^2 + (y'_i - y_j)^2}. \quad (2)$$

- *Scaling α* : Obtained by computing the ratio of enclosed area of the reference shape ($A_{reference}$) over the area of target shape (A_{target})

$$\alpha = \frac{|A_{reference}|}{|A_{target}|}, \quad (3)$$

where $|S|$ represents the cardinality of the set S .

- *Rotation matrix $R(\theta)$* : This is defined as

$$R(\theta) = \begin{bmatrix} \cos(\theta) & -\sin(\theta) \\ \sin(\theta) & \cos(\theta) \end{bmatrix}. \quad (4)$$

Note that this alignment method is also used in adjusting the shape prior model to the same translation, rotation, and scale as the shape of the curve under current evolution process.

Each shape in the training set is embedded as the zero level set of a higher dimensional surface Ψ_i . The points on the surface encode the distance to the nearest point in the shape, with negative distance inside and positive distance outside the shape. The function Ψ_i , which is a matrix (or a signed distance map) and of the same size as the training shape template, is defined as

$$\Psi_i = \begin{cases} 0 & S, \\ -D((x, y), S) & (x, y) \in \Omega_f, \\ D((x, y), S) & (x, y) \in \Omega_b \end{cases} \quad (5)$$

where $D((x, y), S)$ is a function that returns the minimum Euclidean distance between the grid pixel (x, y) and the shape contour S , Ω_f is the foreground region, and Ω_b is the background region. To convert these level set

functions into feature vectors, they are rearranged into column vectors and form a matrix $M = \Psi_1, \Psi_2, \dots, \Psi_n$, where M is a $N \times n$ matrix, N is the dimensionality of the feature vectors and n is the number of training samples. We apply PCA to reduce the dimensionality of the data. Assuming that the PDF of the training set is Gaussian, then the probability density function (PDF) associated with the projected data is given as:

$$P(\mathbf{x}_{pca}) = \frac{1}{(2\pi)^{p/2} |\mathbf{\Lambda}_p|^{1/2}} \exp\left(-\frac{1}{2} \mathbf{x}_{pca}^T \mathbf{\Lambda}_p^{-1} \mathbf{x}_{pca}\right), \quad (6)$$

where \mathbf{x}_{pca} represents projected data from PCA and $\mathbf{\Lambda}_p$ is a diagonal matrix containing the first p eigenvalues. Minimizing the PDF in Equation (6) gives us the shape prior ψ_o . We encode the similarity transform $A_s = (\alpha, R, T)$ of the shape prior into the model to give $\psi(\mathbf{x}_{pca}) = \psi_o(A_s(\mathbf{x}_{pca}))$.

3.2 Ellipsoidal Shape Prior

In this paper, we have considered Ellipses as the 2-D shape of interest. We have generated a training set of 30 ellipses by changing the size of a principle axis with a Gaussian probability function and applied PCA on the SDFs of 30 training ellipses. We extract the one principle component that explains 98% of the variance in the shape of the ellipses and the shape function corresponding to the mean and the eigenmode of variation of the training set (Figure 1).

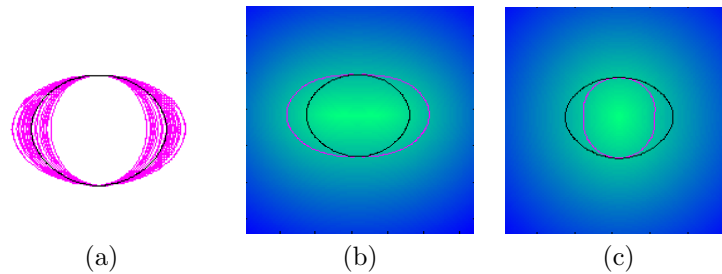


Figure 1. (a) The set of 30 aligned training ellipses with the mean ellipse shown via a dotted line. Figures 1(b) and 1(c) represent reconstructed ellipses from PCA with mean shape shown via a black contour.

4. INTEGRATED ACTIVE CONTOUR FORMULATION

4.1 Shape Term

Each shape in the training set is embedded as the zero level set of a higher dimensional surface. A signed distance function (SDF) is used to encode the distance of the shape contour to the nearest point in the shape space. F_{shape} is a functional that depends on the AC providing the boundaries. This functional evaluates the shape difference between the level set ϕ and the zero level set of the shape function ψ . It should be noted that PCA applied on aligned SDFs of a training set produces shape functions very close to that of the SDFs. The level set formulation of the shape functional is given as:

$$F_{shape} = \int_{\Omega} (\phi(\mathbf{x}) - \psi(\mathbf{x}))^2 |\nabla \phi| \delta(\phi) d\mathbf{x}, \quad (7)$$

where ϕ is a level set function, ψ is the shape prior, $\delta(\cdot)$ is the Dirac delta function, and $\delta(\phi)$ is the contour measure on $\{\phi = 0\}$. Since ϕ undergoes a similarity transformation to adjust the pose and scale, we can also write F_{shape} in terms of rotation, translation, and a scaling factor.

The above model introduces the shape prior in such a way that only objects of interest similar to the shape prior can be recovered, and all unfamiliar image structures are suppressed. However, this formulation solves for a single level set consistent with the shape prior. If there are several objects corresponding to the same shape in the scene, this model finds at most *one* object. Often it may not find any matching objects in the scene. Therefore we incorporate a method to deal with the segmentation of multiple objects of similar shape in the scene.

4.2 Region Homogeneity Term

We define a functional to drive the shape model towards a homogeneous intensity region using the shape prior. If our objects of interest have a smooth intensity surface, then the Mumford-Shah (MS) model is the most appropriate model to segment these objects.¹⁰ Since the MS method applied on the AC will extract globally homogeneous regions and our objective is to capture an object belonging to a particular shape space, the best solution is to apply the MS-based force on the shape prior.¹⁰ Indeed, this new force will globally drive the shape prior towards a homogeneous intensity region with the shape of interest. The functional F_{region} can be written with the shape function ψ and statistics of partitioned foreground and background regions, u_{in}, u_{out} :

$$F_{region}(\psi, u_{in}, u_{out}) = \int_{\Omega} \Theta_{in} H_{\psi} d\mathbf{x} + \int_{\Omega} \Theta_{out} H_{-\psi} d\mathbf{x}, \quad (8)$$

where ψ is the shape function, H_{ψ} is the Heaviside function, $\Theta_r = |I - u_r|^2 + \mu|\nabla u_r|^2$ and $r \in \{in, out\}$.

4.3 Combining Shape-Based, Boundary-Based and Region-Based Functionals

We define a synergistic model to address the problem of object segmentation, integrating a geometric shape prior with local and global intensity information within a variational framework:

$$F = F_1 + F_{region}(\psi, u_{in}, u_{out}), \quad (9)$$

$$F_1 = \beta_1 F_{boundary}(C) + \beta_2 F_{shape}(\phi, \psi), \quad (10)$$

where $F_{boundary} = \int_{\Omega} g(f(\mathbf{x}))|\nabla H(\phi)|d\mathbf{x}$, ψ is the shape function of the object of interest given by the PCA (see Section 3.1), g is an edge detecting function and β_1, β_2 are arbitrary positive constants that balance the contributions of the boundary, shape and region terms. The proposed functional F_1 is an extension of the work of Chen, et al.⁶ where we have integrated a new statistical shape model. Writing out Equation (9) in its entirety we have,

$$F(\Phi, \Psi, u_{in}, u_{out}) = \underbrace{\int_{\Omega} (\phi(\mathbf{x}) - \psi(\mathbf{x}))^2 |\nabla \phi| \delta(\phi) d\mathbf{x}}_{Shape+boundary\ force} + \underbrace{\beta_r \int_{\Omega} \Theta_{in} H_{\psi} d\mathbf{x} + \int_{\Omega} \Theta_{out} H_{-\psi} d\mathbf{x}}_{Region\ force} \quad (11)$$

4.4 Formulation to segment multiple objects under mutual occlusion

The level set formulation in Equation (11) is limited in that it allows for segmentation of only a single object at a time. In this work, we incorporate the method presented in¹⁶ into Equation (11). Consider a given image consisting of multiple objects $\{O_1, O_2, \dots, O_m\}$ of the same shape. For the problems considered in this work (nuclei segmentation on histopathology images), all nuclei are assumed to be roughly elliptical in shape. Instead of partitioning the image domain into mutually exclusive regions, we allow each pixel to be associated with multiple objects or the background. Specifically, we try to find a set of characteristic functions χ_f such that:

$$\chi_f(\mathbf{x}) = \begin{cases} 1 & \text{if } \mathbf{x} \in O_f, \\ 0 & \text{if otherwise.} \end{cases} \quad (12)$$

We associate one level set per object in such a way that any $O_k, O_l, k, l \in \{1, 2, \dots, m\}$ are allowed to overlap with each other within the image. These level set components may both be positive within the area of overlap, and enforce the prior on the shapes of objects extracted from the image. We consider a specific case of segmenting two objects within an input image, which is then generalized to N independent familiar objects.

The simultaneous segmentation of two familiar objects with respect to the given shape prior is solved by minimizing the following modified version of Equation (11):

$$\begin{aligned}
 F(\Phi, \Psi, u_{in}, u_{out}) = & \sum_{a=1}^2 \int_{\Omega} (\phi_a(\mathbf{x}) - \psi(\mathbf{x}))^2 |\nabla \phi_a| \delta(\phi_a) d\mathbf{x} + \\
 & \beta_r \int_{\Omega} (\Theta_{in} H_{\chi_1 \vee \chi_2}) d\mathbf{x} + \int_{\Omega} (\Theta_{out} - H_{\chi_1 \vee \chi_2}) d\mathbf{x} \\
 & + \omega \int_{\Omega} H_{\chi_1 \wedge \chi_2} d\mathbf{x} + \sum_{a=1}^2 \int_{\Omega} (\phi_a - \psi_a)^2 d\mathbf{x},
 \end{aligned} \tag{13}$$

where $H_{\chi_1 \vee \chi_2} = H_{\psi_1} + H_{\psi_2} - H_{\psi_1} H_{\psi_2}$, $H_{\chi_1 \wedge \chi_2} = H_{\psi_1} H_{\psi_2}$, $\Phi = (\phi_1, \phi_2)$, and $\Psi = (\psi_1, \psi_2)$. The fourth term penalizes the overlapping area between the two regions being segmented, and it prevents the two evolving level set functions from becoming identical. Minimizing Equation (13) by alternating with respect to dynamic variables, yields the associated Euler-Lagrange equations, parameterizing the decent direction by time $t > 0$.

General case of $N > 2$. The described above method can be generalized for simultaneous segmentation of $N > 2$ independent objects, all of which can leverage the shape prior ψ_a :

$$\begin{aligned}
 F(\Phi, \Psi, u_{in}, u_{out}) = & \sum_{a=1}^N \int_{\Omega} (\phi_a(\mathbf{x}) - \psi(\mathbf{x}))^2 |\nabla \phi_a| \delta(\phi_a) d\mathbf{x} + \\
 & \beta_r \int_{\Omega} (\Theta_{in} H_{\chi_1 \vee \chi_2}) d\mathbf{x} + \int_{\Omega} (\Theta_{out} - H_{\chi_1 \vee \chi_2}) d\mathbf{x} \\
 & + \omega \sum_{a \neq b} \int_{\Omega} H_{\chi_1 \wedge \chi_2} d\mathbf{x} + \sum_{a=1}^N \int_{\Omega} (\phi_a - \psi_a)^2 d\mathbf{x}.
 \end{aligned} \tag{14}$$

5. EXPERIMENTAL DESIGN AND PERFORMANCE MEASURES

5.1 Model Parameters and Data Description

In this paper, for the shape model, we generate a training set of 30 ellipses (nuclei and lymphocytes being elliptical in shape) by changing the size of a principal axis with a gaussian probability function. The manner of choosing the weighting parameters from Equations (9) and (11) is as follows: β_1 is always equal to 1, μ determines the size of the neighborhood where the grey value information is averaged by means of diffusion, β_r is chosen such that the shape prior is attracted towards the region to be segmented, and β_2 is selected in order to allow the active contour to move around the shape prior to capture local boundaries. Level sets are manually initialized and the model assumes that the level sets are strategically placed in the vicinity of the objects.

| | Name | Number |
|-----------|--|--------|
| Dataset 1 | Hematoxylin & Eosin (H&E) stained prostate needle core biopsy images | 14 |
| Dataset 2 | Hematoxylin & Eosin (H&E) stained breast biopsy images | 100 |

Table 2. Description of the different data sets considered in this study.

| | Dataset 1 | | Dataset 2 | |
|---------------------------|---------------|---------------|---------------|---------------|
| Comparative Strategy | No. of Images | No. of Nuclei | No. of Images | No. of Nuclei |
| Detection | 3 | 10 | 25 | 100 |
| Segmentation | 5 | 30 | 37 | 154 |
| Overlap resolution | 6 | 40 | 33 | 250 |

Table 3. Description of the number of studies (detection, segmentation, and overlap resolution) for which this model was evaluated.

Evaluation is done on two different histopathology datasets: prostate cancer and breast cancer cohorts comprising 100 and 14 images respectively. A total of 70 cancer nuclei from 14 images for prostate and 504 lymphocytes from 52 images for breast cancer were manually delineated by an expert pathologist (serving as the ground truth annotation for quantitative evaluation). Qualitative evaluation of the model was visually done on all 114 images.

5.2 Comparative Strategies

We qualitatively and quantitatively compared the segmentation performance with the GAC (Geodesic Active Contour)¹¹ and the Rousson shape based model (RD).⁸ The RD model is a popular region based AC model where the model is driven by the Gaussian distribution of both foreground and background and also involves a shape prior.

5.2.1 Experiment 1: Overlap Resolution

The aim of this experiment was to demonstrate the ability of our scheme to correctly resolve the overlap between all intersecting lymphocytes and nuclei across 114 breast and prostate cancer histopathology images.

5.2.2 Experiment 2: Comparison of our model against the GAC and Rousson-Derich (RD) models in terms of detection accuracy

The aim of this experiment was to compare the detection accuracy of our model over two state-of-the-art AC models, GAC and RD.

5.2.3 Experiment 3: Comparison against GAC and RD model in terms of segmentation accuracy

The aim of this experiment was to compare the segmentation performance in terms of boundary and area overlap metrics compared to the GAC and RD model.

5.3 Performance Measures

5.3.1 Evaluation of Detection Performance

The metrics used to evaluate object detection include: 1) sensitivity (SN); 2) positive predictive value (PPV); and 3) overlap detection ratio (OR) (see Table 4). The detection results from three models (Chan-Vese, our model and RD) are compared to manual detection results obtained from an expert clinician. The SN and PPV values are computed from the true-positive (TP), false-positive (FP), and false-negative (FN) values (TP, FN, FP are subsequently defined):

$$SN = \frac{TP}{TP + FN}, \quad (15)$$

$$PPV = \frac{TP}{TP + FP}. \quad (16)$$

TP refers to the number of lymphocyte nuclei correctly identified while FP refers to the number of objects incorrectly identified as lymphocyte nuclei and FN refers to the number of lymphocyte nuclei missed by the model. The detection results are represented as the centroid of the region enclosed by a closed contour. TP, FP, and FN values are obtained by comparing each centroid generated by the model to manually determined object centroid.

The overlap detection ratio (OR) (Table 2) is computed as follows:

$$OR = \frac{\text{Number of overlaps resolved}}{\text{Total number of overlaps}}.$$

An overlap is characterized by the existence of a common boundary between two objects and in our case may be between two or more lymphocytic nuclei, cancer nuclei, or both.

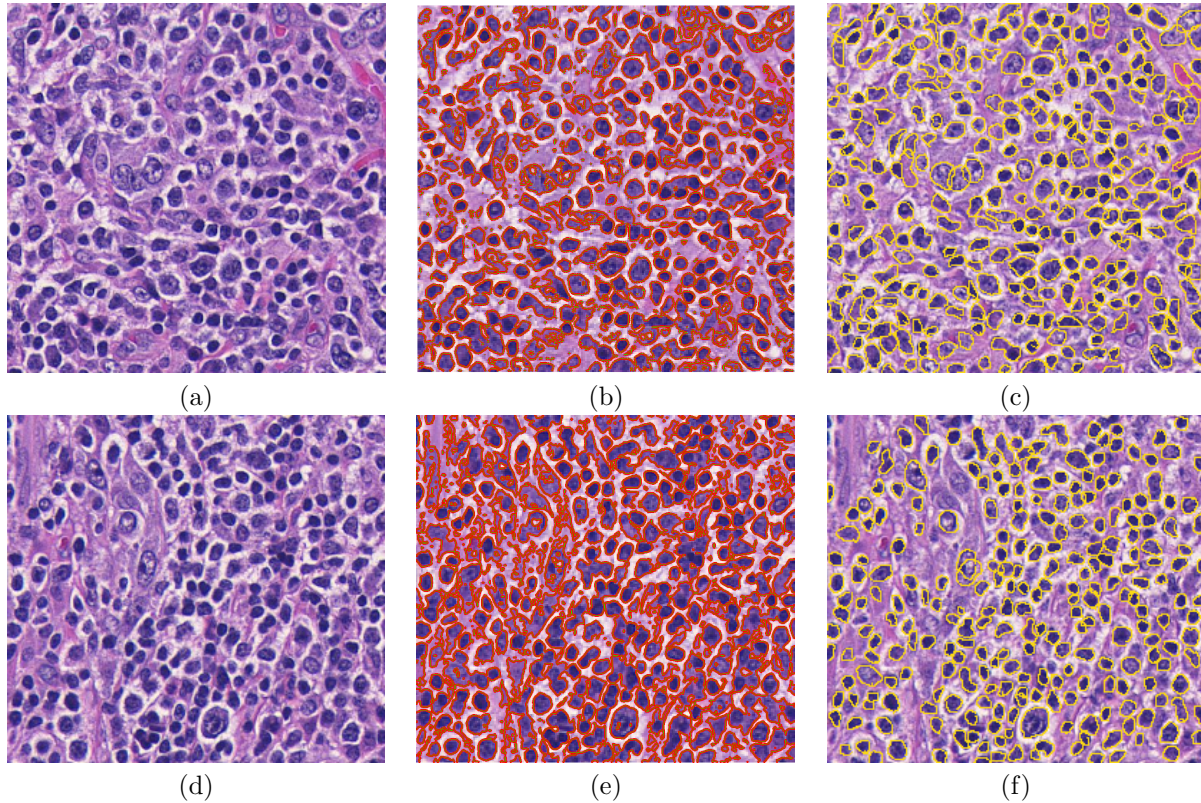


Figure 2. (a), (d) Original histological image. (b), (e) Segmentation results from the Chan-Vese Model. (c), (f) Segmentation results from our model. Note that our model is able to segment intersecting, overlapping nuclei compared to the Chan-Vese model.

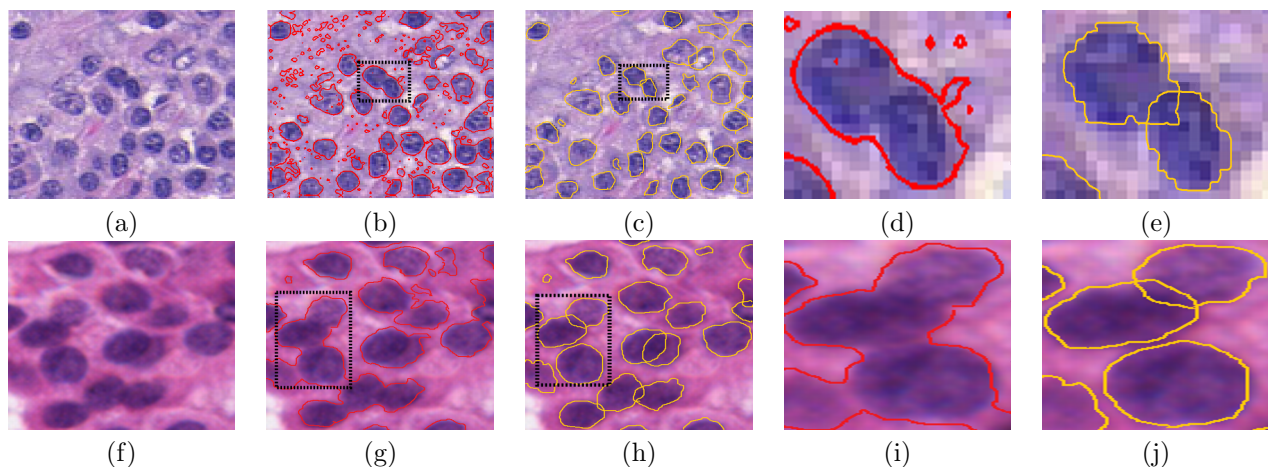


Figure 3. (a), (f) Original histological images corresponding to breast and prostate histology respectively, segmentation results for nuclei and lymphocytes obtained via the (b), (g) Geodesic Active Contour; (c), (h) our integrated AC model; (d), (e) magnified region from (b) and (g); (e), (j) magnified region from (c) and (h).

5.3.2 Evaluation of Segmentation Performance

Segmentation results are compared to manual delineations performed by an expert oncologist (which serves as ground truth for segmentation evaluation) by computing boundary based metrics, namely Hausdorff distance (HD), mean absolute distance (MAD), and area overlap metrics (true positive area (TP_a), false-positive area

(FP_a), true-negative area (TN_a), and false-negative area (FN_a)). The manual delineation is represented as a closed boundary \mathcal{G} .

Since manual delineation of 100 BC and 14 CaP images is tedious and time consuming, the expert was asked to provide manual delineations of 100 nuclei randomly chosen from histology images from the two datasets. For each of the 100 object boundary segmentations, a corresponding value for HD and MAD were obtained. HD and MAD values close to zero correspond to better segmentation. The area overlap metrics are used to compute the sensitivity SN_a , specificity SP_a , positive predictive value PPV_a and the overlap ratio OV_a of the segmentation results for each of the three models. The area overlap metrics are computed as follows:

$$TP_a = \frac{|\mathcal{A}(S) \cap \mathcal{A}(\mathcal{G})|}{\mathcal{A}(\mathcal{G})},$$

$$FP_a = \frac{|\mathcal{A}(S) \cup \mathcal{A}(\mathcal{G}) - \mathcal{A}(\mathcal{G})|}{\mathcal{A}(\mathcal{G})},$$

$$FN_a = \frac{|\mathcal{A}(S) \cup \mathcal{A}(\mathcal{G}) - \mathcal{A}(S)|}{\mathcal{A}(\mathcal{G})}, \text{ and}$$

$$TN_a = \frac{|\mathbf{C} - \mathcal{A}(\mathcal{G})|}{\mathcal{A}(\mathcal{G})}.$$

where $\mathcal{A}(\cdot)$ is the area of the closed boundary. For each image, the set of pixels lying within the manual delineations of the nuclei is denoted as $\mathcal{A}(\mathcal{G})$. $\mathcal{A}(S)$ is the set of pixels whose level set functions are positive, after the convergence of active contour model. The SN_a and PPV_a values are computed in a similar fashion as described in (15) and (16), respectively. SP_a and OV_a values are computed as follows:

$$SP_a = \frac{TN_a}{TN_a + FP_a},$$

$$OV_a = \frac{TP_a}{TP_a + FP_a + FN_a}.$$

6. RESULTS AND DISCUSSION

6.1 Qualitative Results

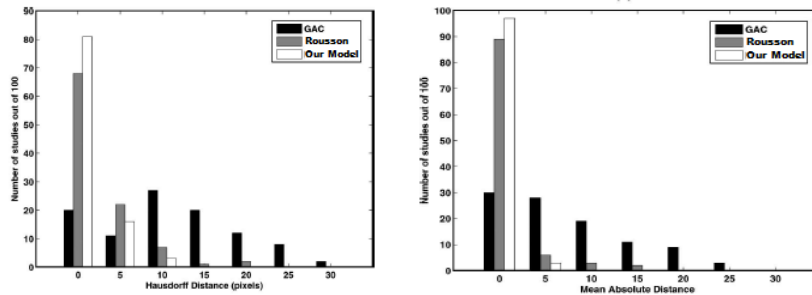


Figure 4. Histogram for (a) HD and (b) MAD for each of the three models. Note that HD and MAD values close to zero correspond to better segmentation. The plot reflects the number of studies (y-axis) for which the HD and MAD values were below a certain number of image pixels (x-axis).

Qualitative results for 2 of the 114 different studies are illustrated in Figures 2 and 3 and reflect the superiority of our model. We evaluate our model on segmenting the images from two different histopathology datasets: prostate cancer and breast cancer. For these data sets, we apply our model for segmenting the gland lumen and

Table 4. Quantitative evaluation of detection results for the 3 models over 100 breast histology images.

| | SN | PPV | OR |
|------------------|-------------|-------------|-------------|
| GAC | 0.20 | 0.58 | 0.022 |
| Rousson | 0.59 | 0.63 | 0.74 |
| Our Model | 0.86 | 0.64 | 0.91 |

Table 5. Quantitative evaluation of segmentation results between GAC, Rousson and our model for 100 lymphocytes.

| | SN_a | SP_a | PPV_a | OV_a | HD | MAD |
|------------------|-------------|------------|-------------|-------------|------------|------------|
| GAC | 0.31 | 0.94 | 0.21 | 0.17 | 11.3 | 7.6 |
| Rousson | 0.79 | 0.88 | 0.58 | 0.49 | 2.9 | 1.5 |
| Our model | 0.80 | 1.0 | 0.86 | 0.72 | 2.1 | 1.1 |

Table 6. Detection performance between the 3 models for each of the dataset.

| | GAC | RD | Our model |
|------------------|-----|-----|------------|
| Dataset 1 | 67% | 71% | 90% |
| Dataset 2 | 65% | 72% | 92% |

lymphocytes, respectively. The results shown in Figures 2 and 3 for lymphocyte segmentation aim to demonstrate the strength of our model in terms of detections, segmentation, and overlap resolution. For both the breast and prostate histology images in Figures 2 and 3 respectively, our model was able to detect and segment lymphocytes and cancer nuclei accurately, compared to the Chan-Vese model.

6.2 Quantitative Results

Results of quantitative evaluation of detection and segmentation performance for each of the three models are shown in Tables 4 and 5. These results reflect the improved performance over Rousson and GAC, respectively. The SN and PPV values listed in Table 4 reflect the efficacy of our model in detecting lymphocytes in BC images and detecting nuclei in prostate images as compared to other two models. A total of 504 cases of overlapping objects were manually identified in 52 images from dataset 2 and our model was able to resolve 465 (92.5%) overlaps.

In terms of segmentation performance, our model easily outperformed both Rousson and GAC models, respectively, in terms of all six segmentation evaluation measures over 100 lymphocytes. One random lymphocyte was chosen from each of the images in the dataset to evaluate segmentation results. Figure 4 shows histogram plots of the HD and MAD values for the three models over 100 lymphocytes for which segmentation evaluation was done. The HD and MAD values for our model were less than 5 pixels for over 95% and 99% of the studies respectively. The statistical measures from the area overlap metrics are summarized in Table 5.

We compare detection results from the GAC model, RD model and our segmentation scheme with respect to segmentation results from manual delineations performed by an expert (ground truth) for a total of 70 nuclei from 14 images for prostate cancer (dataset 1) and 504 lymphocytes from 52 images for breast cancer (dataset 2). We also compared the number of true objects segmented by comparing the foreground regions formed by level sets (where level set > 0). On dataset 2, our model detected 92% true lymphocytes as compare to 65% by GAC and 72% via the Rousson model. We achieved a corresponding 90% lymphocyte detection performance on dataset 1 (see Table 6).

Table 7. p-values of t-test between three models for performance metrics from 114 studies.

| | SN | PPV | OR | SN_a | SP_a | PPV_a | OV_a | HD | MAD |
|--------------------------|-----------------------|----------------------|-----------------------|-----------------------|----------------------|-----------------------|-----------------------|-----------------------|-----------------------|
| GAC/Rousson | 2.6×10^{-34} | 6.1×10^{-3} | 1.8×10^{-14} | 1.1×10^{-16} | 8.1×10^{-3} | 1.9×10^{-15} | 1.9×10^{-17} | 4.5×10^{-16} | 1.5×10^{-13} |
| GAC/Our Model | 1.3×10^{-73} | 1.4×10^{-3} | 1.3×10^{-81} | 6.1×10^{-18} | 8.2×10^{-4} | 2.8×10^{-33} | 1.2×10^{-31} | 3.8×10^{-21} | 2.1×10^{-17} |
| Rousson/Our Model | 1.5×10^{-50} | 6.9×10^{-1} | 1.4×10^{-57} | 9.5×10^{-1} | 1.3×10^{-4} | 7.9×10^{-12} | 1.7×10^{-10} | 4.6×10^{-3} | 1.7×10^{-2} |

6.3 Test of statistical significance between models

For each of the 114 studies, performance evaluation metrics (SN , PPV , SN_a , PPV_a , SP_a , OV_a , HD, and MAD) were compared for every pair of models using the paired t-test under the null hypothesis that there is no significant difference in the values of the metrics between all three models. The null-hypothesis was rejected for p -value ≤ 0.05 (see Table 7). For almost every performance metric (except for two), our model showed a statistically significant improvement compared to GAC and Rousson models.

7. CONCLUDING REMARKS

We presented a novel segmentation method that uses boundary and region based active contours with a statistical shape prior to accurately detect and segment multiple overlapping objects in the scene. Furthermore, we presented our model in a multiple level set formulation to segment multiple objects under mutual occlusion. Specifically, our model was able to overcome the inability of popular segmentation models in resolving revolving overlapping objects. One limitation of our model is that requires user intervention in initialization of the level set and in future work, we intend to incorporate an automated initialization method thereby minimizing the extent of user intervention.

We applied our hybrid model for segmentation and detection of lymphocytes, gland lumen, and nuclei in BC and prostate histopathology imagery. Our results show that our model appears outperform state-of-the-art active contours and statistical shape models. Our model was able to segment overlapping lymphocytes and lumen with more than 90% accuracy.

The ability to automatically and accurately segment lymphocytes in BC histopathology images may serve to be useful in quantitatively studying lymphocytic infiltration and its relation to BC prognosis. The relationship between the presence of lymphocytic infiltration and good prognosis has also been observed in other pathologies such as ovarian cancer.¹⁸ Hence, the algorithm developed in this study might also be similarly employed in building an automated prognostic prediction scheme for other diseases.

Acknowledgment

This work was made possible via grants from the Wallace H. Coulter Foundation, National Cancer Institute (Grant Nos. R01CA136535-01, R01CA14077201, and R03CA143991-01), and The Cancer Institute of New Jersey. We would like to thank Dr. John E. Tomaszewski and Dr. Michael D. Feldman from the Pathology Department at the Hospital of the University of Pennsylvania and Dr. Shridar Ganesan at the Cancer Institute of New Jersey for providing the prostate histology imagery and ground truth annotation.

REFERENCES

- [1] T.F. Cootes, D. Cooper, C.J. Taylor and J. Graham, "Active Shape Models - Their Training and Application." *Computer Vision and Image Understanding*. Vol. 61, No. 1, Jan. 1995, pp. 38-59.
- [2] Robert W. Veltri, Sumit Isharwal, M. Craig Mille, "Nuclear Roundness Variance Predicts Prostate Cancer Progression, Metastasis, and Death: A Prospective Evaluation With up to 25 Years of Follow-Up After Radical Prostatectomy," *The Prostate.*, vol. 70, 133m-1339, 2010.
- [3] Fatakawala, H, Xu, J, Basavanahally, A, Bhanot, G, Ganesan, S, Feldman, M, Tomaszewski, J, Madabhushi, A, "Expectation Maximization driven Geodesic Active Contour with Overlap Resolution (EMaGACOR): Application to Lymphocyte Segmentation on Breast Cancer Histopathology," *Biomedical Engineering, IEEE Transactions on*, vol.57(7), pp. 1676-1689, 2010.
- [4] M. Kass, A. Witkin and D. Terzopoulos, "Snakes: active contour models", *International Journal of Computer Vision*, pp. 321-331, 1987.
- [5] Wen Fang and Kap Luk Chan, "Statistical Shape Influence in Geodesic Active Contours", *IEEE Conference on Computer Vision and Pattern*, vol.40, no.8, pp. 2163-2172, 2007.
- [6] Tony Chan, "Level set based shape prior segmentation", *IEEE Computer Society Conference on Computer Vision and Pattern Recognition*, vol 2, pp.1164-1170, 2005.

- [7] N. Paragios and R. Deriche, "Unifying boundary and region-based information for geodesic active tracking", *IEEE Conference on Computer Vision and Pattern Recognition* vol. 2, 1999, pp. 300-305.
- [8] M. Rousson and N. Paragios, "Shape priors for level set representation", *European Conference on Computer Vision*, pp. 78-92, 2002
- [9] X. Bresson, P. Vandergheynst and J.P. Thiran, "A priori information in image segmentation: energy functional based on shape statistical model and image information", *IEEE Int. Conf. on Image Processing*, vol. 3, September 2003, pp. 425-428.
- [10] T.F. Chan, L.A Vese, "Active contours without edges", *IEEE Trans. on Image Processing*, vol. 10, no. 2, pp. 266-277, 2001.
- [11] V. Caselles, R. Kimmel and G. Sapiro, "Geodesic active contours", *Int.J. Comput. Vision*, vol 22, no.1, pp. 61-79, 1997.
- [12] S. Kichenassamy, A. Kumar, P. Olver, A. Tann and A.J. Yezzi, "Conformal curvature flows: From phase transitions to active vision", *In Archive for Rational Mechanics and Analysis*, vol. 134, pp. 275-301, 1996.
- [13] Doyle, S, Hwang, M, Shah, K, Madabhushi, A, Tomasezewski, J, Feldman, M, "Automated Grading of Prostate Cancer using Architectural and Textural Image Features", *International Symposium on Biomedical Imaging (ISBI)*, pp. 1284-87, 2007
- [14] Basavanahally, A, Ganesan, S, Agner, S, Monaco, J, Feldman, M, Tomaszewski, J, Bhanot, G, Madabhushi, A, "Computerized Image-Based Detection and Grading of Lymphocytic Infiltration in HER2+ Breast Cancer Histopathology," *Biomedical Engineering, IEEE Transactions on*, vol.57 (3), pp. 642-653, 2010.
- [15] S. Osher and J. A. Sethian, "Fronts propagating with curvature- dependent speed: algorithms based on Hamilton-Jacobi formulations," *Journal of Computational Physics.*, vol. 79, no. 1, pp. 12-49, 1988.
- [16] Zhang et al. "Segmenting multiple familiar objects under mutual occlusion." *ICIP*, 2006.
- [17] G. Coukos "Intratumoral T Cells, Recurrence, and Survival in Epithelial Ovarian Cancer." *New England journal of medicine*, 2003.
- [18] Gurcan, M, Boucheron, L, Can, A, Madabhushi, A, Rajpoot, N, Yener, B, "Histopathological Image Analysis: A Review", *IEEE Reviews in Biomedical Engineering*, vol. 2, pp. 147-171, 2009.
- [19] Madabhushi, A, "Digital Pathology Image Analysis: Opportunities and Challenges (Editorial)", *Imaging in Medicine*, vol. 1(1), pp. 7-10, 2009.